Wear 408–409 (2018) 190–199

Contents lists available at ScienceDirect

Wear

journal homepage: www.elsevier.com/locate/wear

Friction and wear of Pd-rich amorphous alloy ($Pd_{43}Cu_{27}Ni_{10}P_{20}$) under dry and ionic liquid (IL) lubricated conditions

Jaeho Lee[a], Muyang He[a], Chang-Dong Yeo[a,*], Golden Kumar[a], Zhonglue Hu[a],
Edward L. Quitevis[b], Vidura D. Thalangamaarachchige[b]

[a] Department of Mechanical Engineering, Texas Tech University, Lubbock, TX 79409, USA
[b] Department of Chemistry & Biochemistry, Texas Tech University, Lubbock, TX 79409, USA

ARTICLE INFO

Keywords:
Glassy metal
Ionic liquids
Tribofilm
Friction
Wear
Reciprocating ball-on-disc

ABSTRACT

Palladium (Pd) based metallic glass has attracted attention because of its superior tribological performance thereby becoming a potential material to solve contact induced failures and improve the reliability of many engineering applications. In this study, Pd-rich metallic glass ($Pd_{43}Cu_{27}Ni_{10}P_{20}$) was synthesized, and novel experiments were designed to obtain fundamental insight into its friction and wear behavior. The tribological performance of amorphous (i.e., Pd-rich amorphous alloy) and crystalline (i.e., pure crystalline Pd) palladium under dry and lubricated contact condition was investigated through the reciprocating ball-on-disc tests. The ionic liquid (IL), i.e., 1-nonyl-3-methylimidazolium bis[(trifluoromethane)sulfonyl]amide ($[C_9C_1im][NTf_2]$), was applied as a lubricant. Under the controlled contact conditions (i.e., sliding velocity, contact load, and environment temperature), the in-situ friction and ex-situ wear were measured and compared quantitatively. First, at dry contact conditions, the amorphous Pd alloy showed much lower coefficient of friction and wear than the crystalline Pd. Three wear mechanisms (delamination, abrasive and adhesive wear) were identified on the crystalline Pd, whereas the amorphous Pd alloy showed single dominant wear mechanism, namely abrasion. Next, when the IL lubricant was applied to the contact interface, it significantly improved the friction and wear of both amorphous and crystalline Pd samples. Only abrasive wear mechanism was observed on both types of Pd samples. In particular, the IL lubrication was more effective to the crystalline Pd sample partly because of the tribofilm formation on the surface.

1. Introduction

Metallic glasses have been receiving increasing attention in the field of surface engineering due to their unique properties such as high material strength, hardness, excellent corrosion and wear resistance, and durability [1–5]. Therefore, metallic glasses have been applied in various engineering applications including dry bearings in aerospace and automobile industries [2], gears in manufacturing devices [3], medical instruments [4], structural materials [3], and surface coatings [4,5].

The friction and wear behavior of metallic glasses during sliding contact have been studied by many researchers [6–17]. Parlar et al. [8] investigated the tribological performance of Zr-based metallic glass with respect to load and speed under dry sliding contact. It was reported that the metallic glass showed better friction characteristics than structural materials. Prakash [12] evaluated the abrasive type of wear behavior for Fe, Co, and Ni-based metallic glasses and found that their wear characteristics were slightly superior or close to that of stainless steel. For the case of a copper-based metallic glass, its tribological performance could be improved by controlled annealing treatments [13]. Rahaman et al. [14] investigated the relationship between phase transition and tribological properties of metallic glass under dry sliding contact and reported that frictional heat played a vital role in friction and wear behavior of the metallic glass. Blau [15] examined the sliding friction and wear of a Zr-based metallic glass, whose results were compared to those of 303 stainless steel and Ni-200. It was observed that the Zr-based metallic glass showed better tribological performance under dry contact conditions, whereas it had higher friction and wear rate under lubricated conditions (lubrication by 15W40 diesel oil). The wear behavior of a metallic glass composite was also evaluated through dry sliding contact test [16], and it was reported that the composite showed higher wear rates but lower coefficient of friction compared to a monolithic metallic glass. Despite extensive studies on friction and wear of metallic glasses, further research is required because new

---

* Corresponding author.
E-mail address: changdong.yeo@ttu.edu (C.-D. Yeo).

https://doi.org/10.1016/j.wear.2018.05.017
Received 18 October 2017; Received in revised form 26 May 2018; Accepted 27 May 2018

metallic glasses are being designed to improve their functionality. In addition, not many studies have been conducted on metallic glasses under lubricated-contact conditions, even though the contact interfaces of practical engineering components are under several types of lubricants [16,17]. Recently ionic liquids (ILs) have been studied as lubricants or additives due to their thermochemical stability and miscibility with organic compounds. When an IL is applied onto metal surfaces, an ordered layered structure is formed [18,19]:anions are strongly bonded and anchored to the metal surface through polar interaction thus enabling efficient separation of counteracting metal surfaces, with the cations forming a layer over anions, thereby providing a mobile characteristic with lower shear and friction. At light load conditions, the adsorbed layered structure keeps the moving parts separated, preventing direct solid contacts. Under high load conditions, the layered IL can be broken down leading to chemical reactions with metal surfaces promoted by the high contact pressure and temperature at the interface. Depending on the chemical compositions, these reactions can help to develop tribofilm on the metal surfaces that favorably reduces the friction and wear [20–23].

Imidazolium ILs with short-alkyl chain cations such as 1-butyl-3-methylimidazolium ($[C_4C_1im]^+$) or 1-ethyl-3-methylimidazolium ($[C_2C_1im]^+$) and $[PF_6]^-$ or $[BF_4]^-$ as anion were commonly used in earlier studies of ILs as lubricants [19,24,25]. When imidazolium-based ILs were applied to the interface of steel/steel or aluminum/steel, it was observed that the ILs could be broken down at extreme contact conditions [26–29]. The breakdown products were primarily those of the anions ($[PF_6]^-$ or $[BF_4]^-$), which reacted with the exposed metal surface forming a protective tribofilm. The X-ray photoelectron spectroscopy (XPS) measurements on the wear scar showed that the composition of the tribofilms were mainly metal fluorides, phosphates, and B_2O_3. However, as ILs with these ions tend to be hydrophilic, they can develop tribocorrosion when adsorbed water reacts with $[PF_6]^-$ or $[BF_4]^-$ anions producing unwanted corrosive compounds such as HF. This problem can be mitigated by using bis[(trifluoromethane)sulfonyl] amide ($[N(CF_3SO_2)_2]^-$ or $[NTf_2]^-$) as an anion. ILs containing $[NTf_2]^-$ have better hydrolytic and thermal stability compared to ILs containing $[BF_4]^-$ and $[PF_6]^-$, and they typically produce metal fluorides on contacting metal surfaces [29–31]. Our choice of $[C_9C_1im][NTf_2]$ also takes advantage of the fact that longer alkyl chain lengths moderate the reaction of the anion with water, thereby reducing corrosion, further improving the wear performance [27–29,32].

In this study, amorphous ($Pd_{43}Cu_{27}Ni_{10}P_{20}$) and pure crystalline Pd samples were prepared and their tribological performance was investigated through the reciprocating ball-on-disc tests at ambient temperature under dry and lubricated contact. The IL $[C_9C_1im][NTf_2]$ was synthesized and applied to the contact interface as a lubricant, because it was expected to give better wear performance than other earlier ILs. The resulting friction, wear, and the formation of tribofilm on metal surfaces were systematically examined.

2. Sample preparation and instrumentation

2.1. Metal alloy samples based on palladium: amorphous vs. crystalline

The Pd-rich amorphous alloy ($Pd_{43}Cu_{27}Ni_{10}P_{20}$) was prepared by vacuum melting and water quenching [33], while flat discs of crystalline Pd (99.999%) were prepared by cold rolling. Subsequently, the amorphous alloy was reshaped into a disc by thermoplastic forming at 355 °C. The amorphous nature of the disc was verified by differential scanning calorimeter (DSC) analysis. The both crystalline and amorphous Pd discs were polished with 4000 grit sand papers to ensure similar surface roughness for friction and wear tests. After polishing, the amorphous state of Pd was verified using X-ray diffraction (XRD). As shown in Fig. 1, no crystalline peaks were observed in both samples.

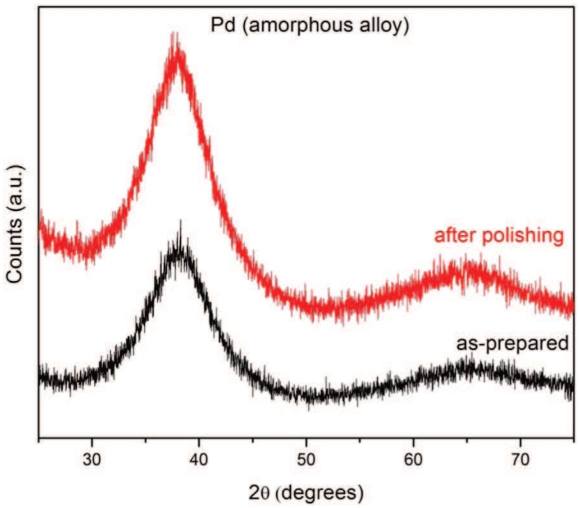

Fig. 1. XRD patterns of Pd-rich amorphous alloy in the as-prepared state and after polishing.

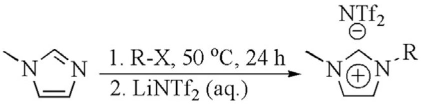

Fig. 2. Generic synthesis of $[C_9C_1im][NTf_2]$ with R = C_9H_{19}.

2.2. Synthesis of bis[(trifluoromethane)sulfonyl]amide $[C_9C_1im][NTf_2]$

The IL $[C_9C_1im][NTf_2]$ was synthesized following the general procedure summarized below in Fig. 2, which is based on procedures published by Bartsch and coworkers [34,35] with modifications. A detailed description of the synthesis and purification of $[C_9C_1im][NTf_2]$ is given in greater detail, along with the NMR analysis confirming the final product, in a previous publication [36].

2.3. Material characterization of metal specimens

2.3.1. Surface roughness

In general, friction and wear behaviors during sliding-contact tests can be affected by material properties and the topography of the contacting surfaces. Before performing the reciprocating sliding contact test, the surface roughness, surface energy, and hardness of the two metal specimens were measured.

As shown in Fig. 3, the surface topographies of the two metal specimens were obtained by using an Asylum MFP-3D Atomic Force Microscope (AFM). The AFM images were then used to calculate the surface roughness value of the specimens. The resulting root-mean-square (RMS) roughness value was 19.64 nm for pure crystalline Pd and 12.35 nm for Pd-based glassy alloy (amorphous Pd) specimens, respectively. From the topography images and roughness values, it could be found that the crystalline Pd specimen was slightly rougher than the amorphous one.

2.3.2. Surface energy: dispersive and polar components

The surface energy of the two metal specimens was obtained using contact-angle measurements. To determine the dispersive and polar components of surface free energy, two reference liquids were applied – one was methylene iodide (dispersive energy (γ_l^d) = 51 mJ/m^2), which interacts only with the dispersive force, and the other was deionized (DI) water (dispersive energy (γ_w^d) = 21.8 mJ/m^2 and polar energy (γ_w^p) energy = 51 mJ/m^2), which interacts with both dispersive and polar forces.

Fig. 4 shows a representative image of the contact angle

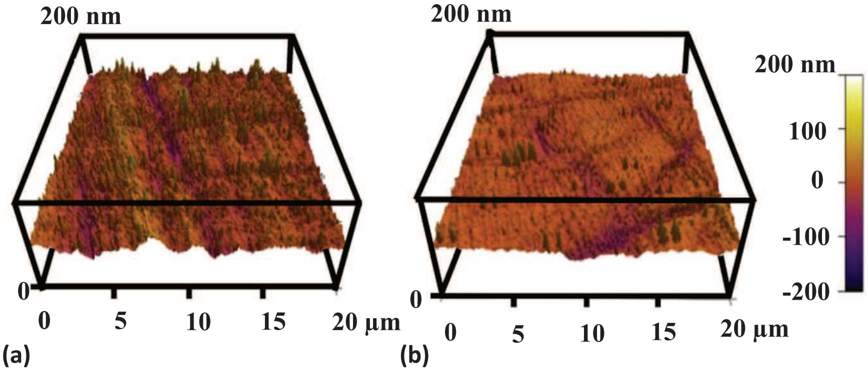

Fig. 3. Surface topographies obtained by Asylum MFP-3D AFM: (a) pure crystalline Pd and (b) Pd-based metallic glass.

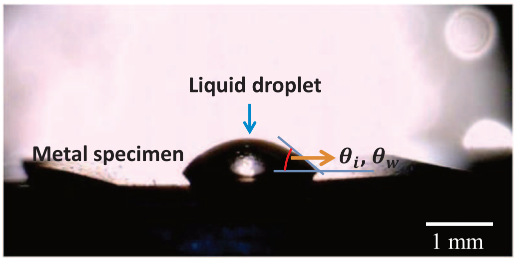

Fig. 4. The calculation of surface energy using contact angle measurement: θ_i = contact angle by methylene iodide and θ_w = contact angle by DI water.

measurement in this experiment. Using the measured contact angle values for the two reference liquids (θ_i for methylene iodide and θ_w for DI water), the dispersive (γ_s^d), and polar (γ_s^p) surface energy of the metal specimens can be determined by the following equations [37]:

$$\gamma_s^d = \gamma_l^d(1+\cos\theta_i)^2/4 \tag{1}$$

$$\gamma_s^p = \left[(\gamma_w^d + \gamma_w^p)(1+\cos\theta_w) - 2\sqrt{\gamma_s^d\gamma_w^d}\right]^2/4\gamma_w^p \tag{2}$$

For the reliable surface energy measurement, the contact angles were obtained at five different spots on each specimen surface. The resulting total surface energy value was 44.45 mJ/m^2 for the crystalline Pd and 61.12 mJ/m^2 for the amorphous Pd alloy. Table 1 summarizes the measured dispersive and polar components of surface free energy for the two metal specimens. Comparing the surface energy between the two metal specimens, it was found that the polar surface energy component of the amorphous sample was ~ 2.5 times higher than that of the crystalline Pd. This indicates that the higher surface energy of amorphous Pd alloy is mostly attributed to its polar component rather than the dispersive one.

2.3.3. Material hardness

The hardness was measured using the Rockwell superficial hardness tester (BUEHLER) with 15 T scale and a 1/16 steel ball tip. For each metal specimen, the measurement was performed at three different spots, from which the averaged hardness value was obtained. The measured Rockwell superficial hardness value was 78.5 (Brinell hardness = 118 HB) for the crystalline Pd and 90.8 (= 240 HB) for the amorphous Pd alloy.

Table 1
The measured surface energy values for crystalline and amorphous Pd.

Sample		Palladium	
		Crystalline	Amorphous
Surface Energy (mJ/m^2)	Dispersive	37.47	44.29
	Polar	6.98	16.83
	Total	44.45	61.12

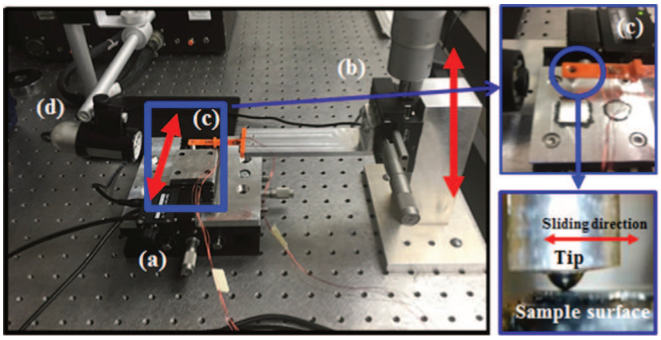

Fig. 5. The schematic of the sliding contact tester: (a) sample stage, (b) micro-stage to control normal force, (c) tip holder and cantilever with two strain gauges, and (d) high resolution digital camera.

2.4. Experimental procedures

Fig. 5 shows the newly developed reciprocating ball-on-disc tester used in this study, which consists of four parts: (a) a sample plate attached to a motorized stage (i.e., Zaber™ High Precision Motorized Stage) that enables horizontal reciprocating motion of metal samples, (b) a micro-stage to control the applied normal force, (c) a tip (= 304 stainless steel ball with a 2 mm diameter and hardness = 300 HB) holder and cantilever with two strain gauges to measure the in-situ normal and tangential (or frictional) forces during the reciprocating sliding contact test, and (d) a digital microscope with 220× magnification, which was focused on the trailing edge of the contact area to monitor the initiation of physical surface damage of metal samples.

Under the controlled contact load and speed, the reciprocating ball-on-disc contact test was carried out in dry and IL lubricated conditions. Considering engineering applications operate in slow speed and high-pressure contact, such as large gears and slow speed roller bearings that typically experience boundary lubrication [40,41], the test conditions (i.e., contact load and speed) in this study were selected and controlled to give boundary lubrication during the reciprocating ball-on-disc test. In the experiment, the contact speed (or sliding speed) was varied from 3 mm/s to 7 mm/s with the stroke of 5 mm, and the normal contact force changed from 15 gf to 25 gf. The applied contact conditions satisfied boundary lubrication during the sliding contact according to the Stribeck curve factor ($\eta V/W$) [38]. The details are described in Section 3.2. In every test configuration, a new steel ball was used to enable consistent contact conditions, and the total test time was ~ 90 min. Accordingly, the sliding distance was ~ 15 m for the speed of 3 mm/s and ~ 35 m for the sliding speed of 7 mm/s. For the lubricated contact test, the IL was applied onto the metal specimen surface and the steel ball tip was immersed into the IL. To obtain a reliable comparison of friction and wear behavior, five repeated tests were performed at each test configuration. All sliding contact tests were carried out in a clean room (class 100) to avoid any errors from contaminants and particles, where the environmental temperature and humidity were 23 °C and RH < 30%, respectively.

The in-situ normal and friction forces were measured by the two directional force sensors (i.e., the calibrated strain gauges in normal and tangential directions) on the cantilever, while the quantitative analysis of wear was obtained through the surface morphology measurements with a scanning electron microscope (SEM) and a Contour GT surface profiler (Bruker). In addition, the formation of a tribofilm and material transfer behavior on the contacting surfaces were investigated through X-ray photoelectron spectroscopy (PHI 5000 VersaProbe XPS system) with ion gun sputtering (beam voltage = 500 V, time = 30 s), where the applied X-rays were monochromatic Al Kα X-rays and the binding energy position of adventitious carbon was 284.6 eV. The sputtering depth was estimated from the etching rate of the standard SiO_2 film and the element composition of the sample surfaces were obtained from the MultiPak software.

3. Results and discussion

3.1. Friction and wear under dry contact: amorphous Pd alloy vs. crystalline Pd

Fig. 6 summarizes the measured coefficient of friction (COF) with respect to the sliding distance for the crystalline Pd (solid line with diamond symbol) and amorphous Pd alloy (dashed line with square symbol) samples under dry contact condition. It was observed that the amorphous Pd alloy sample showed a much lower friction coefficient (i.e., COF: 0.2–0.4) than the crystalline Pd sample (i.e., COF: 0.6–0.8) for all the contact conditions. The friction coefficient of both crystalline and amorphous samples increased sharply in the early stage of sliding contact, which might be attributed to the removal of the initial oxide layer and foreign materials on the sample surfaces. The friction coefficient then reached the steady-state value. The steady-state friction coefficient of the amorphous Pd alloy was ~ 2 times lower than that of the crystalline Pd. Upon examining the effects of contact load and speed on the resulting COF values, the COF was found to be more dependent on the contact load rather than the contact speed.

Using the post-experiment samples, the wear behavior of the crystalline and amorphous Pd alloy samples was analyzed using SEM/EDS and 3D scanning of surface topography. Fig. 7 shows a comparison of 3D morphology of wear tracks between crystalline and amorphous Pd sample. Similar to the results of friction in Fig. 6, it was observed that the crystalline Pd sample showed a much deeper and wider scratch than the amorphous Pd alloy. The averaged scratch width and depth are 306.8 μm and 11.6 μm for the crystalline Pd and 50.8 μm and 0.14 μm for the amorphous Pd, respectively. It is noted that as the initial surface topography of the crystalline Pd (RMS roughness = 19.64 nm) was rougher than the amorphous Pd alloy (RMS roughness = 12.35 nm), the friction and wear of the crystalline Pd could be higher at the early stage of sliding contact. However, considering the size of wear track for the post-experiment samples was much larger than the roughness value, the difference of the initial roughness would have limited effects on the steady-state COF value and the resulting wear mechanisms of the two types of Pd samples.

The wear mechanism of each sample was examined using SEM and EDS data. For the case of crystalline Pd sample, three wear mechanisms were identified from the SEM images, i.e., delamination, abrasive and adhesive wear. First, as shown in Fig. 8(a), the worn surface of the crystalline Pd sample showed clear subsurface cracks and flakes that are the typical evidence of delamination wear. When the harder ball makes repeated sliding contacts over the softer crystalline Pd, the high contact stress can cause plastic deformation on the crystalline Pd and change its subsurface microstructure, which can result in nucleation of subsurface cracks. Accordingly, these cracks can be propagated to the surface by the following contacts thereby producing flakes and wear particles. Second, the worn surface in Fig. 8(a) also showed the grooves in the direction of sliding contact, which are typically produced by the abrasion process. From the EDS data obtained at the worn surface, the detected elements were mostly found to be from the crystalline Pd without external compositions or material transfer from the ball tip.

Third, considerable plastic deformations and material smearing

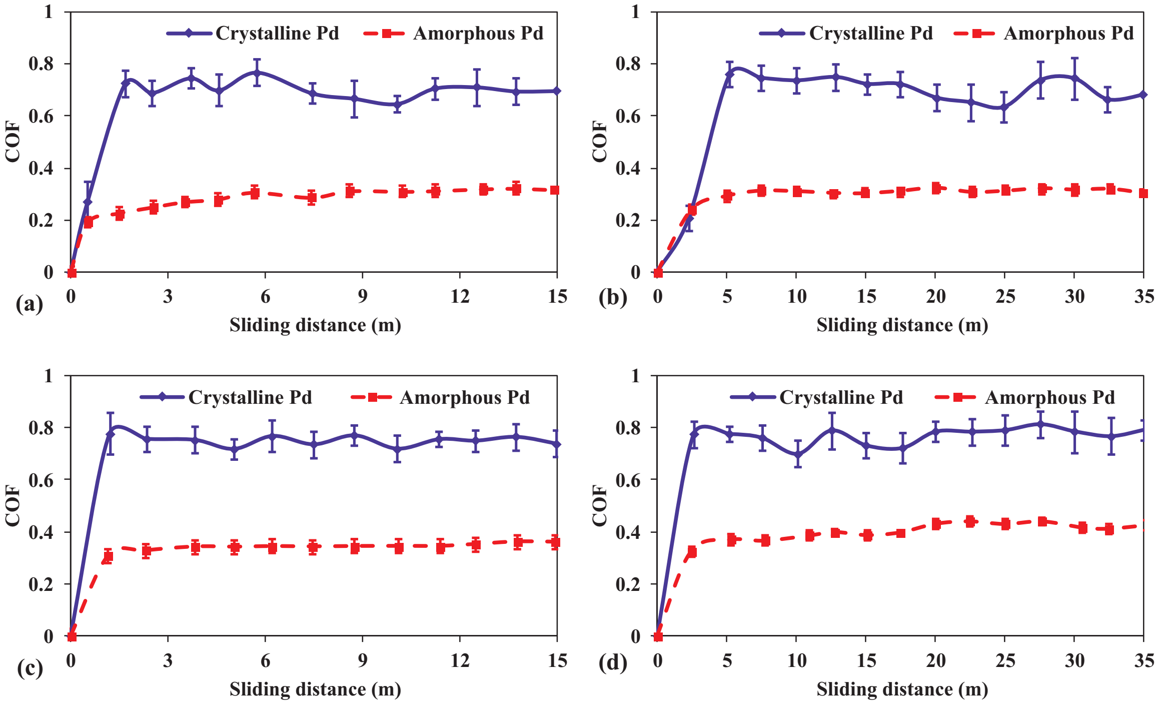

Fig. 6. The measured friction coefficient with respect to sliding distance in dry condition at the temperature and humidity of 23 °C and RH < 30%, respectively: (a) 15 gf and 3 mm/s, (b) 15 gf and 7 mm/s, (c) 25 gf and 3 mm/s, (d) 25 gf and 7 mm/s.

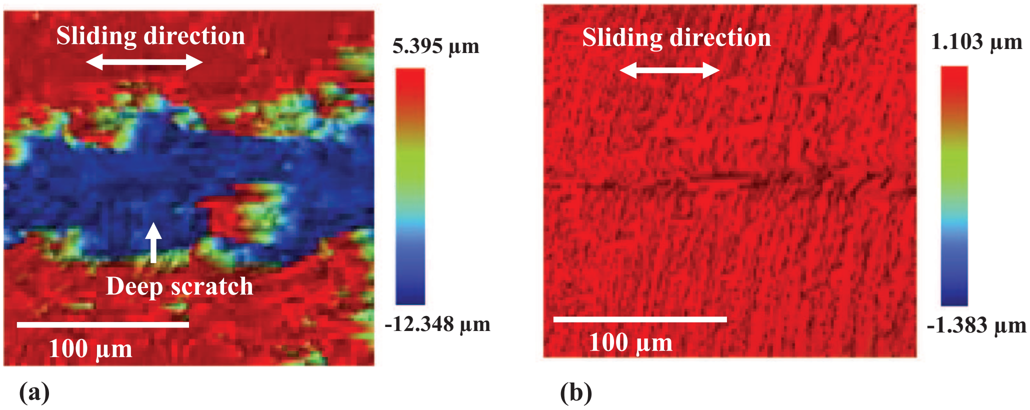

Fig. 7. Optical 3D profilometry scans on wear track under dry contact: (a) crystalline Pd and (b) amorphous Pd alloy.

marks on the crystalline Pd surface in Fig. 8(a) implied another wear mechanism, i.e., adhesive wear. The worn surface of the tested ball tip was examined through SEM/EDS analysis. Fig. 8(b) shows the SEM image in BSE mode for the ball tip surface, and the EDS data were obtained at two representative areas in the wear scar, i.e., black (1) and white (2) spots. It was observed that the elements on the black spot (1) was mostly from the ball tip including small amounts of Pd, whereas the dominant element on the white spot (2) was Pd. The distribution of

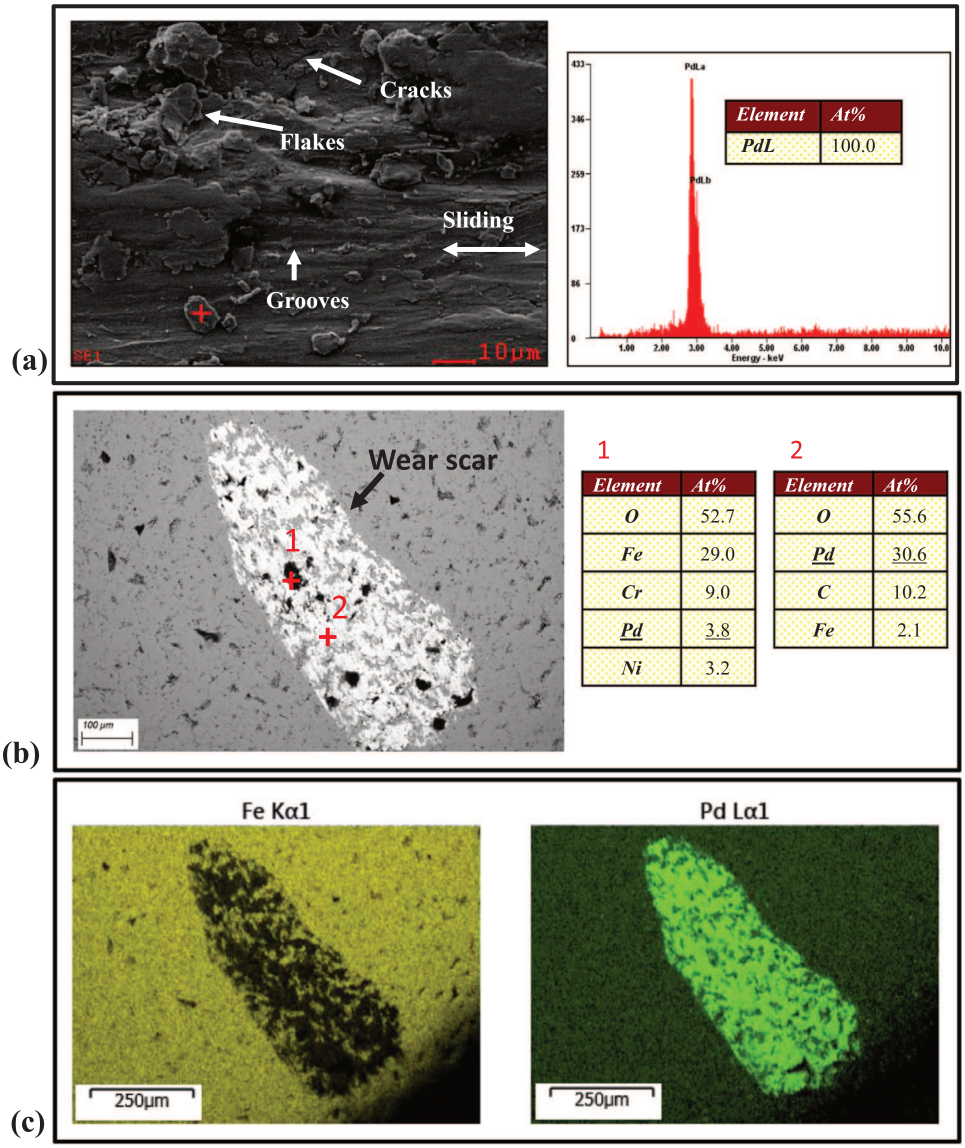

Element	At%
PdL	100.0

1

Element	At%
O	52.7
Fe	29.0
Cr	9.0
Pd	3.8
Ni	3.2

2

Element	At%
O	55.6
Pd	30.6
C	10.2
Fe	2.1

Fig. 8. SEM and EDS analysis for the crystalline Pd and the ball tip samples after dry sliding contact test: (a) SEM image (SE mode) of the worn crystalline Pd surface including its EDS data, (b) SEM image (BSE mode) of the ball tip surface including its EDS data, and (c) element mapping images for Fe and Pd.

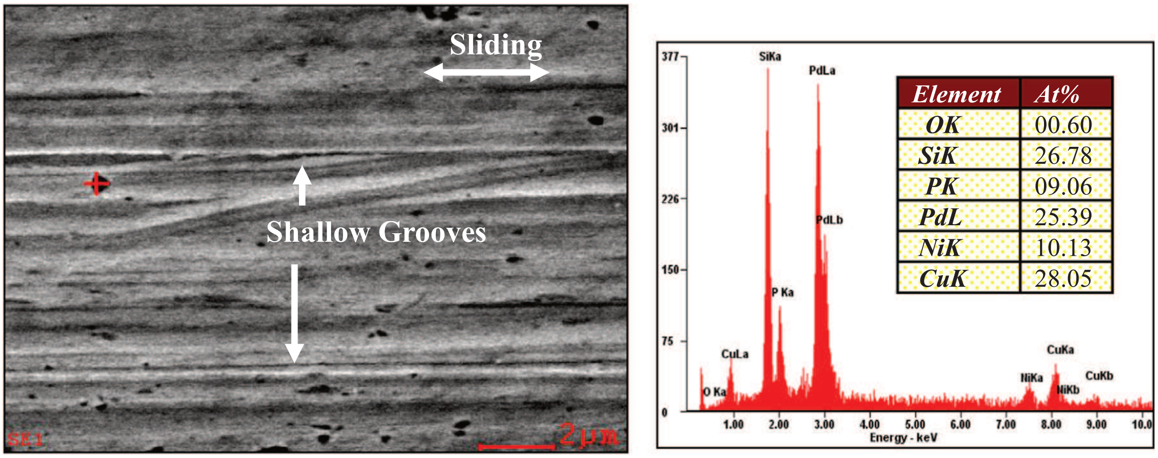

Fig. 9. SEM and EDS analysis on the worn surface of the amorphous Pd alloy after dry sliding contact test.

major element for the ball tip (Fe) and the crystalline Pd was further evaluated using the element mapping as shown in Fig. 8(c). It was found that Pd element was widely spread over the wear scar area, which supports the adhesive-wear process whereby high plastic deformation and adhesion led to material transfer from the crystalline Pd sample to the harder ball tip surface during the repeated sliding contact.

Compared to the crystalline Pd sample, the amorphous Pd alloy showed single dominant wear mechanism, i.e., abrasion. As shown in Fig. 9, the worn surface of the amorphous Pd alloy showed many shallow grooves in the direction of sliding contact. Given that the amorphous structure does not have a specific slip plan, crack nucleation and propagation during the sliding contact does not easily occur. The EDS data on the worn surface also confirmed that the detected elements were mostly from the amorphous Pd alloy. Regarding the wear behavior of the tested ball tip sample, it was hard to locate the wear scar in microscope view. Considering the amorphous Pd alloy had narrower and shallower wear tracks (Fig. 7) without clear material smearing marks on the worn surface (Fig. 9), it is expected that the ball tip surface would have much smaller size of wear scar with limited amount of material transfer.

Based on the morphology of wear tracks, the wear coefficient (K) was calculated using the Archard equation, i.e., $K = VH/WL$ (V = wear volume, H = hardness, W = contact load, L = sliding distance). Fig. 10 summarizes the resulting K values for crystalline Pd (Fig. 10(a)) and amorphous Pd alloy (Fig. 10(b)) at all tested conditions, and it could be observed that the amorphous Pd alloy has superior wear resistance compared to the crystalline Pd. The wear coefficient of the crystalline Pd was on the order of 10^{-3}, while the amorphous Pd alloy was on the order of 10^{-6}. It is noted that not only is the amorphous Pd alloy harder than the pure crystalline Pd but that the amorphous structure does not have a specific slip plane. Therefore, the lower wear volume and higher wear resistance of the amorphous Pd alloy sample can be attributed to its material and structural properties.

Lastly, we also examined the resulting friction and wear of the pure crystalline and amorphous Pd alloy samples (Figs. 6–10) with respect to their surface energy values in Table 1, and found that within the test conditions, the surface energy did not show a clear relationship with the COF, wear coefficient, and wear mechanisms.

3.2. *Friction and wear under IL lubricated contact: amorphous vs. crystalline Pd*

The IL [C_9C_1im][NTf_2] was applied onto the surface of the crystalline Pd and amorphous Pd alloy samples, and the reciprocating ball-on-disc tests were carried out with the same contact load and speed conditions as in the dry contact tests. The $\eta V/W$ factor in the Stribeck diagram was calculated to determine the lubrication regime during the sliding contact, where η is the IL viscosity, V the sliding speed and W the normal load [26]. The viscosity of the IL at 23 °C is 100 mPa s [39]. It was found that the highest $\eta V/W$ factor was 0.005 at the contact speed of 7 mm/s and the applied load of 15 gf, which is less than the upper limit of boundary lubrication, i.e., 0.01. Accordingly, it is reasonable to assume that the lubricated sliding contact in this experiment is within the boundary lubrication regime.

Fig. 11 shows the measured COF values at each test configuration under IL lubrication. Similar to the results of dry contact test in Fig. 6, the amorphous Pd alloy sample showed lower a friction coefficient (i.e., COF: 0.15–0.20) than the crystalline Pd sample (i.e., COF: 0.20–0.25) for all the contact conditions. However, the effectiveness of IL lubrication on the reduction of COF value was different for the two metal samples. Compared to the amorphous Pd alloy, the crystalline Pd

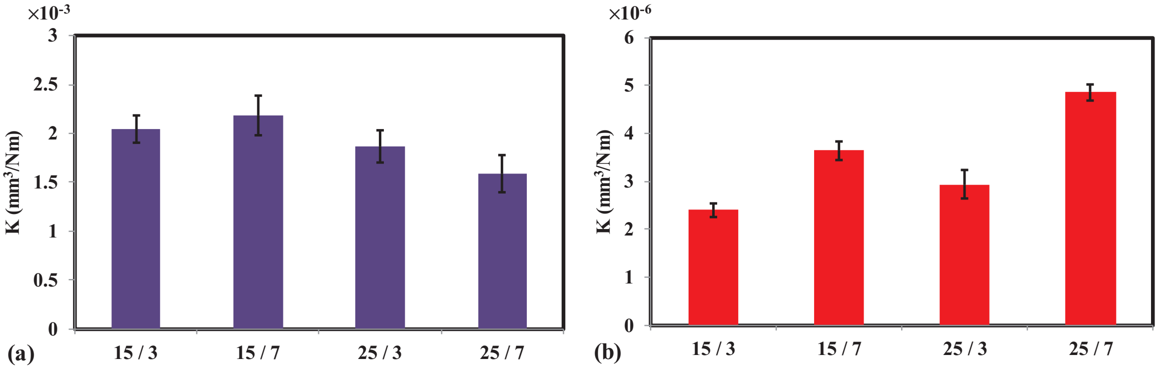

Fig. 10. Wear coefficient K of (a) crystalline Pd and (b) amorphous Pd alloy under dry contact condition.

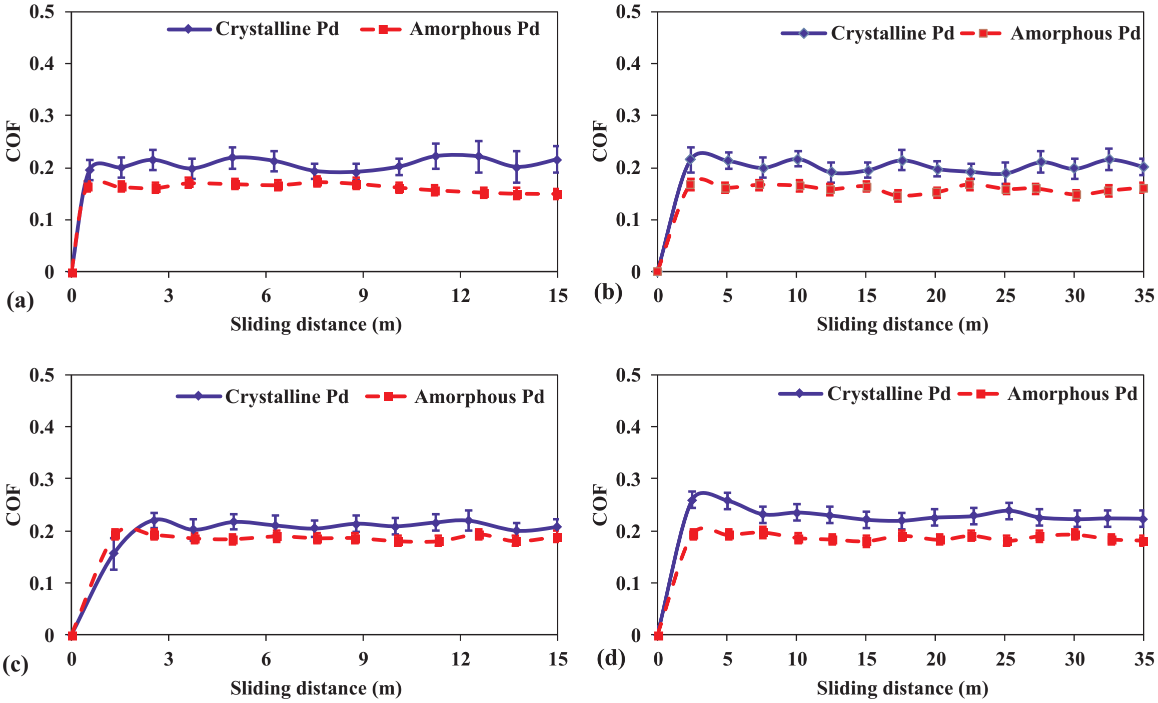

Fig. 11. The measured friction coefficient with respect to sliding distance with IL lubrication at the temperature and humidity of 23 °C and RH < 30%, respectively: (a) 15 gf and 3 mm/s, (b) 15 gf and 7 mm/s, (c) 25 gf and 3 mm/s, (d) 25 gf and 7 mm/s.

showed more dramatic reduction of the COF value from 0.6 to 0.8 at dry contact to 0.15–0.20 at IL lubricated contact, which we attribute to tribofilm formation on the crystalline Pd surface under IL lubricated contact. The mechanism of tribofilm formation is described in the following Section 3.3. Examining the change of COF value with respect to the contact load and speed in Fig. 11, it was also observed that the COF value under IL lubrication showed more dependence on the applied load rather than the speed.

The wear behavior of the crystalline and amorphous Pd samples was examined through 3D profilometry (Fig. 12 (a) and (b)) and SEM and images (Fig. 12 (c) and (d)). The size of wear track from the IL lubricated contact was much smaller than that from the dry contact. The average scratch width and depth were are 81.3 µm and 0.47 µm for the crystalline Pd and 32.5 µm and 0.01 µm for the amorphous Pd, respectively. Interestingly, a single dominant wear mechanism was identified for both the crystalline and amorphous Pd samples, i.e., abrasion. As seen in Fig. 12(c) and (d), the worn surfaces of the two metal samples showed many shallow grooves in sliding direction without clear delamination mark. Compared to the dry contact condition, the IL lubricant layer provides less solid-to-solid contact between the ball-tip and metal-disc surfaces thus developing less contact stress, whose value might not be enough to change the subsurface microstructure and crack nucleation. For this reason, the wear behavior under the IL-lubricated condition is mainly driven by the abrasion process. It is noted that due to the softer material characteristics, the crystalline Pd sample generates a step or edge like plastic deformation on the wedge of the grooves (Fig. 12(c)). Regarding the tested ball tip sample, similarly it was hard to locate the wear scar in microscope view because of much less wear and limited material transfer during lubricated sliding contact.

The wear coefficient *K* was also calculated based on Archard equation. As shown in Fig. 13, the wear coefficient of the crystalline Pd was on the order of 10^{-5}, while the value of the amorphous Pd alloy was on the order of 10^{-7}. The difference of the wear coefficient between crystalline and amorphous Pd samples was decreased from ~ 3 orders at dry contact to ~ 2 orders at IL lubricated contact.

3.3. *Formation of tribofilm on crystalline and amorphous Pd surface*

After the sliding contact experiment under IL lubricant, the Pd samples were cleaned using isopropyl alcohol. Then, XPS measurements were performed to analyze the formation of the tribofilm on the contacting surfaces. In XPS, the ion gun sputtering technique was applied to make a depth profiling of the sample surface as shown in Fig. 14, which enabled investigation of the chemical compositions at the subsurface regions. With the beam voltage of 500 V and the sputtering time of 0.5 min the estimated sputtering depth was 2.16 nm. For comparison, the XPS measurement was carried out on both worn and fresh non-contact surfaces at three different spots (1, 2, and 3).

Table 2 summarizes the analysis of XPS spectra for the crystalline Pd sample, especially the fluorine (F) and sulfur (S) peaks which are elements from the $[NTf_2]^-$ anion of the IL. The binding energy (BE) of the carbon (C) peak in Table 2 provides a reference for establishing the accuracy of the positions of the other two peaks. The C peak occurs at 284 eV, which is consistent with it being associated with carbon in C-C bonds of adventitious C (284.8 eV). We attribute the difference of 0.8 eV between the measured value and the accepted value to systematic error. Therefore positions of the F and S peaks should be increased by 0.8 eV to account for this error.

Firstly, for the post-experiment surfaces without the ion-gun sputtering, it was observed that elements specific to the composition of the IL, i.e., F and S, were detected on the both worn and non-contact area, which are attributed to IL residue still present even after the cleaning process. The value of 168 eV for the position of the S peak is similar to the value for S bonded to O atoms in a sulfate anion as in Na_2SO_4 (~ 169 eV). This peak can therefore be assigned to S atoms in the sulfonyl moieties in the $[NTf_2]^-$ anion of the IL residues. The value of 688 eV for the BE of the F peak is similar to the value for an organic fluoride. This peak can therefore be assigned to F atoms in the CF_3 group in the $[NTf_2]^-$ anion of the IL residues. When the first ion-gun sputtering was applied to the sample surface, F and S were eliminated from the non-contact zone of crystalline Pd sample, because the IL residues on the sample surface are easily removed during the ion-gun sputtering process. However, S was still detected on the worn surface zone. Then, on

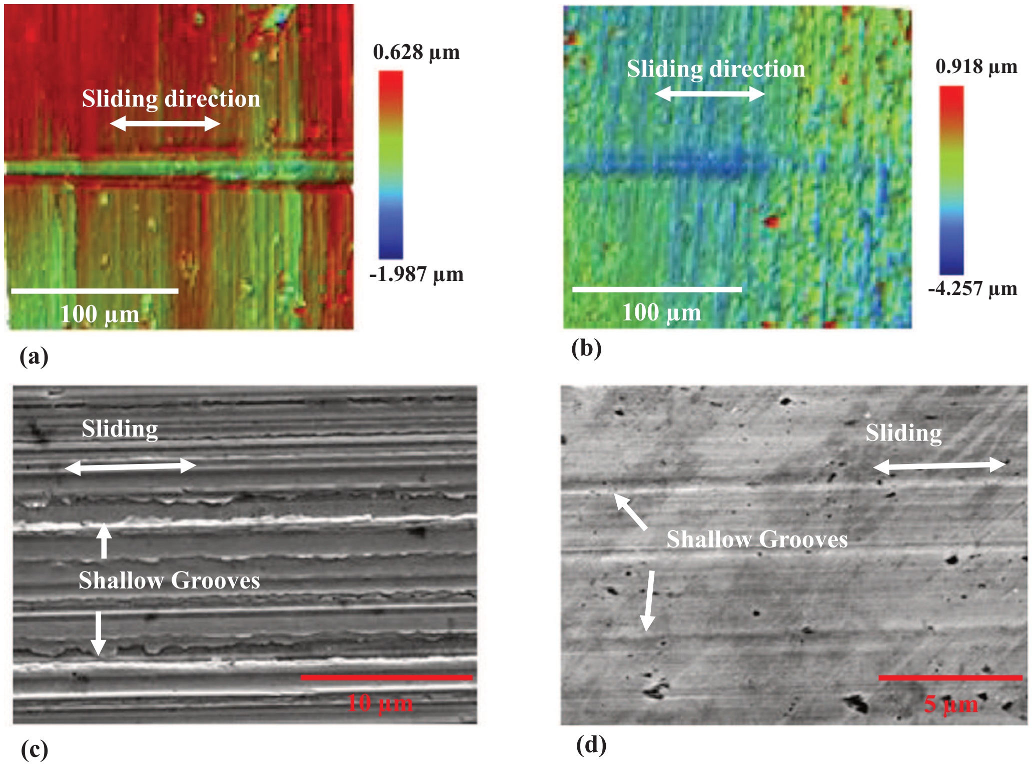

Fig. 12. Morphologies of worn surfaces for the crystalline Pd ((a) and (c)) and the amorphous Pd alloy ((b) and (d)) under IL lubrication: 3D profilometry scanned image ((a) and (b)) and SEM micrographs ((c) and (d)).

the second ion-gun sputtering, it was observed that no S was detected on the spot 1 and 3, but spot 2 still showed the IL element of S.

In the case of spot 2, before sputtering, two S peaks are present. The S peak at 167.2 eV is associated with S atoms in the sulfonyl moiety of the $[NTf_2]^-$ anion. The interesting feature in the XPS spectrum is the peak at 162.4 eV, which can be assigned to a metal sulfide, presumable PdS. After the first ion-gun sputtering, the peak at 167.2 eV disappears, which is consistent with the peak being due to IL residue. However, the peak at 162.4 eV, which is associated with a metal sulfide (e.g. PdS), is still present even after the second ion-gun sputtering.

These results clearly indicate that crystalline Pd during sliding contact under IL lubrication results in the creation of the tribofilm layer on the contact area. The estimated sputtering depth of 2.16 nm indicates that the tribofilm thickness of the crystalline Pd sample is greater than 4.32 nm. Therefore, the XPS data confirmed that the tribofilm on the crystalline Pd was formed by the chemical reactions between Pd and IL lubricant (mostly anions), which could be beneficial to its tribological performance in the following contacts.

On the other hand, in the case of amorphous Pd, there were no F and S peaks found on either worn or non-contact surface zone. It is noted that crystalline Pd is more reactive than amorphous Pd, because in the case of crystalline Pd the sliding contact can create edges and steps on the contacting surface as shown in Fig. 12(c). It is generally expected that exposed atoms at freshly generated edges and steps tend to be more reactive to adsorbed molecules [45]. Therefore, enhanced edge/stepped reactivity with higher friction force can explain more reactivity of crystalline Pd and less reactivity of amorphous Pd with the IL.

3.3.1. *Mechanism for sulfide versus fluoride film formation in Pd/IL system*

If one assumes that the tribofilm to be ionic in nature with the bonding involving the Pd^{2+} ion, the most common charged state of Pd, it can be expected that sulfide film formation to be favored over fluoride film formation because of the larger coulombic interaction between Pd^{2+} and S^{2-} than between Pd^{2+} and F^-. The fact that the coulombic interaction is greater for a Pd^{2+}/S^{2-} ion-pair than for a Pd^{2+}/F^- ion-pair is supported by a back-of-the-envelope calculation

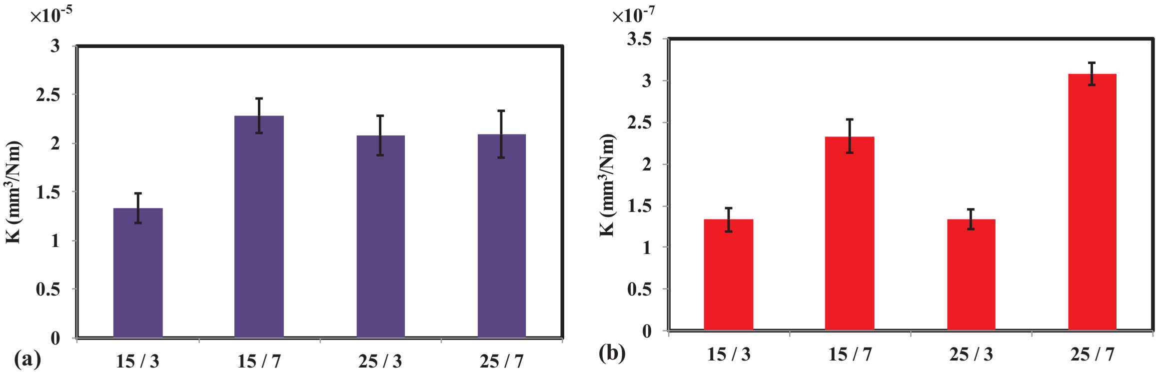

Fig. 13. Wear coefficient *K* of (a) crystalline Pd and (b) amorphous Pd alloy under IL lubricated condition.

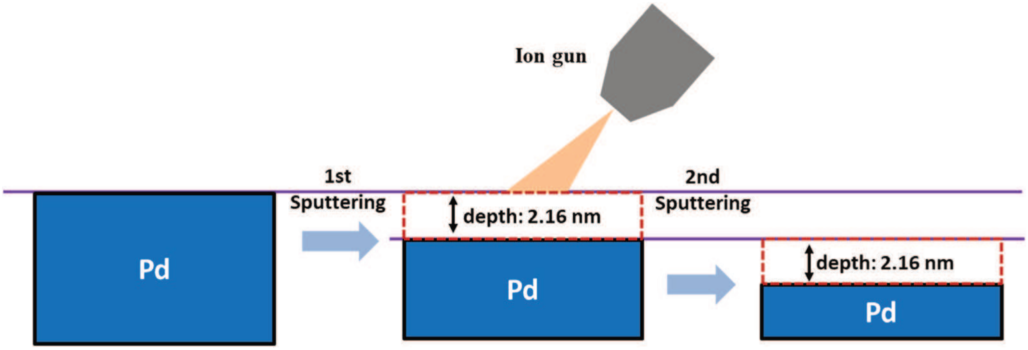

Fig. 14. Schematic of ion gun sputtering technique to examine the chemical composition at subsurface regions (beam voltage: 500 V, time: 0.5 min).

Table 2
Analysis of bind energies of C, S, and F peaks for crystalline Pd sample under IL lubrication after sliding contact.[a]

Sample	C (eV)	S (eV)	F (eV)
Crystalline Pd + IL, Non-Contact			
NC, NS, Spot 1	284	168.	688
NC, S1, Spot 1	284	NP	NP
NC, S2, Spot 1	284	NP	NP
Crystalline Pd + IL, Contact			
C, NS, Spot 1	284	168	688
C, S1, Spot 1	284	161.6	NP
C, S2, Spot 1	284	NP	NP
C, NS, Spot 2	284	162.4, 168	broad (682–689)
C, S1, Spot 2	284	162.4 - broad	NP
C, S2, Spot 2	284	162.4, narrow	NP
C, NS, Spot 3	284	162.4, 167.2	687-broad
C, S1, Spot 3	284	162	NP
C, S2, Spot 3	284	NP	NP

[a] NC – non-contact, C – contact, NS- no sputter, S1, S2 – first and second sputter; NP – no peak.

using the equation:

$$U_{coulomb} \sim \frac{q_+ q_-}{(r_+ + r_-)}, \tag{3}$$

where the radii of the ions $r_+ = 64$ pm for Pd^{2+} ($q_+ = 2$), $r_- = 184$ pm for S^{2-}($q_- = -2$), and $r_- = 133$ pm for F^- ($q_- = -1$) [42]. Substituting these radii values in Eq. (3), we can obtain: $U_{coulomb}(Pd^{2+}\text{-}S^{2-}) \approx 1.6 U_{coulomb}(Pd^{2+}\text{-}F^-)$.

Furthermore, the fact that sulfide-tribofilm formation is favored over fluoride-tribofilm formation can also be rationalized on the basis of Pearson's hard-soft acid-base (HSAB) theory [43]. Whether a Lewis acid or base is hard or soft is dependent on its charge, size, and polarizability. The theory provides a qualitative understanding of the factors that determine chemical properties or drive chemical reactions involving Lewis acids and bases. It is based on the simple rule (Pearson's principle) that hard acids prefer to bind to hard bases and soft acids prefer to bind to soft bases [44]. Moreover, the bonding in the adduct will tend to be ionic in the case of a hard acid and hard base, but covalent in the case of a soft acid and soft base. Therefore Pd^{2+}, a soft acid, will tend to bind to S^{2-}, a soft base, rather than with F^-, a hard base, with the bonding in the adduct, PdS, being primarily covalent.

4. Conclusions

The objective of this study was to investigate the friction and wear of Pd-rich amorphous alloy under dry and IL-lubricated conditions, whose results were compared to those of crystalline pure Pd. Using the reciprocating ball-on-disc tribometer, the in-situ COF values were measured at the controlled contact loads and speeds. The wear coefficient was calculated based on the Archard equation, while the wear mechanism was analyzed through SEM and EDS data. The primary new findings concerning the nature of dry and IL-lubricated wear in the two types of Pd sample were:

1) The amorphous Pd alloy had much lower COF and wear coefficient values than the pure crystalline Pd at both dry and IL-lubricated conditions.
2) Under dry sliding contact, the amorphous Pd alloy showed predominantly abrasion wear, whereas the crystalline pure Pd was worn through three wear mechanisms, i.e., delamination, abrasive and adhesive wear. However, under IL-lubricated sliding contact, a single dominant wear mechanism, i.e., abrasive wear, was identified on both Pd specimens.
3) When the IL $[C_9C_1im][NTf_2]$ was applied as lubricants, the friction and wear of crystalline Pd showed more improvement than the amorphous Pd alloy, which can partially be explained by the tribofilm formation on the crystalline Pd sample. The existence of tribofilm was verified through the XPS measurements with the ion-gun sputtering technique.

Acknowledgements

GK and ZH would like to acknowledge financial support from National Science Foundation through awards CMMI-1663568 and CMMI-1653938.

References

[1] R.C. Tam, C.H. Shek, Abrasion resistance of Cu based bulk metallic glasses, J. Non-Cryst. Solids 347 (1–3) (2004) 268–272.
[2] D.R. Maddala, R.J. Hebert, Sliding wear behavior of Fe50− xCr15Mo14C15B6Erx (x= 0, 1, 2 at%) bulk metallic glass, Wear 294 (2012) 246–256.
[3] J.J. Kruzic, Bulk metallic glasses as structural materials: a review, Adv. Eng. Mater. 18 (8) (2016) 1308–1331.
[4] J.B. Cheng, X.B. Liang, Z.H. Wang, B.S. Xu, Dry sliding friction and wear properties of metallic glass coating and martensite stainless coating, Tribol. Int. 60 (2013) 140–146.
[5] S.S. Joshi, S. Katakam, H. Singh Arora, S. Mukherjee, N.B. Dahotre, Amorphous coatings and surfaces on structural materials, Crit. Rev. Solid State Mater. Sci. 41 (1) (2016) 1–46.
[6] A.L. Greer, W.N. Myung, Abrasive wear resistance of bulk metallic glasses, MRS Online Proc. Libr. Arch. 644 (2000).
[7] E. Fleury, S.M. Lee, H.S. Ahn, W.T. Kim, D.H. Kim, Tribological properties of bulk metallic glasses, Mater. Sci. Eng.: A 375 (2004) 276–279.
[8] Z. Parlar, M. Bakkal, A.J. Shih, Sliding tribological characteristics of Zr-based bulk metallic glass, Intermetallics 16 (1) (2008) 34–41.
[9] H. Wu, I. Baker, Y. Liu, X. Wu, P.R. Munroe, Effects of environment on the sliding tribological behaviors of Zr-based bulk metallic glass, Intermetallics 25 (2012) 115–125.
[10] M.L. Rahaman, L.C. Zhang, H.H. Ruan, Effects of environmental temperature and sliding speed on the tribological behaviour of a Ti-based metallic glass, Intermetallics 52 (2014) 36–48.
[11] B.T. Jang, S.S. Kim, S. Yi, Wear behaviors of a Fe-based amorphous alloy in ambient atmosphere and in distilled water, Met. Mater. Int. 20 (1) (2014) 55–61.
[12] B. Prakash, Abrasive wear behaviour of Fe, Co and Ni based metallic glasses, Wear 258 (1–4) (2005) 217–224.
[13] D.R. Maddala, A. Mubarok, R.J. Hebert, Sliding wear behavior of Cu50Hf41. 5Al8. 5

bulk metallic glass, Wear 269 (7–8) (2010) 572–580.
[14] M.L. Rahaman, L.C. Zhang, H.H. Ruan, Understanding the friction and wear mechanisms of bulk metallic glass under contact sliding, Wear 304 (1–2) (2013) 43–48.
[15] P.J. Blau, Friction and wear of a Zr-based amorphous metal alloy under dry and lubricated conditions, Wear 250 (1–12) (2001) 431–434.
[16] A. Ayyagari, T.W. Scharf, S. Mukherjee, Dry reciprocating sliding wear behavior and mechanisms of bulk metallic glass composites, Wear 350 (2016) 56–62.
[17] M. Bakkal, Sliding tribological characteristics of Zr-based bulk metallic glass under lubricated conditions, Intermetallics 18 (6) (2010) 1251–1253.
[18] A. Mohammad, Inamuddin (Eds.), Green Solvents II: Properties and Applications of Ionic Liquids, Springer, Netherlands, 2012, pp. 203–233.
[19] I. Minami, Ionic liquids in tribology, Molecules 14 (6) (2009) 2286–2305.
[20] A. Morina, A. Neville, Understanding the composition and low friction tribofilm formation/removal in boundary lubrication, Tribol. Int. 40 (10–12) (2007) 1696–1704.
[21] A. Erdemir, G. Ramirez, O.L. Eryilmaz, B. Narayanan, Y. Liao, G. Kamath, S.K. Sankaranarayanan, Carbon-based tribofilms from lubricating oils, Nature 536 (7614) (2016) 67.
[22] S. Yazawa, I. Minami, B. Prakash, Reducing friction and wear of tribological systems through hybrid tribofilm consisting of coating and lubricants, Lubricants 2 (2) (2014) 90–112.
[23] A. Morina, A. Neville, M. Priest, J.H. Green, ZDDP and MoDTC interactions and their effect on tribological performance–tribofilm characteristics and its evolution, Tribol. Lett. 24 (3) (2006) 243–256.
[24] A.E. Somers, P.C. Howlett, D.R. MacFarlane, M. Forsyth, A review of ionic liquid lubricants, Lubricants 1 (1) (2013) 3–21.
[25] Y. Zhou, J. Qu, Ionic liquids as lubricant additives: a review, ACS Appl. Mater. Interfaces 9 (4) (2017) 3209–3222.
[26] C. Ye, W. Liu, Y. Chen, L. Yu, Room-temperature ionic liquids: a novel versatile lubricant, Chem. Commun. 21 (2001) 2244–2245.
[27] H. Wang, Q. Lu, C. Ye, W. Liu, Z. Cui, Friction and wear behaviors of ionic liquid of alkylimidazolium hexafluorophosphates as lubricants for steel/steel contact, Wear 256 (1–2) (2004) 44–48.
[28] A.E. Jiménez, M.D. Bermudez, P. Iglesias, F.J. Carrión, G. Martínez-Nicolás, 1-N-alkyl-3-methylimidazolium ionic liquids as neat lubricants and lubricant additives in steel–aluminium contacts, Wear 260 (7–8) (2006) 766–782.
[29] Z. Mu, F. Zhou, S. Zhang, Y. Liang, W. Liu, Effect of the functional groups in ionic liquid molecules on the friction and wear behavior of aluminum alloy in lubricated aluminum-on-steel contact, Tribol. Int. 38 (8) (2005) 725–731.
[30] Q. Lu, H. Wang, C. Ye, W. Liu, Q. Xue, Room temperature ionic liquid 1-ethyl-3-hexylimidazolium-bis (trifluoromethylsulfonyl)-imide as lubricant for steel–steel contact, Tribol. Int. 37 (7) (2004) 547–552.
[31] X. Liu, F. Zhou, Y. Liang, W. Liu, Tribological performance of phosphonium based ionic liquids for an aluminum-on-steel system and opinions on lubrication mechanism, Wear 261 (10) (2006) 1174–1179.
[32] Y. Cao, Y. Chen, X. Sun, Z. Zhang, T. Mu, Water sorption in ionic liquids: kinetics, mechanisms and hydrophilicity, Phys. Chem. Chem. Phys. 14 (35) (2012) 12252–12262.
[33] M. Hasan, N. Kahler, G. Kumar, Shape-controlled metal–metal and metal–polymer janus structures by thermoplastic embossing, ACS Appl. Mater. Interfaces 8 (17) (2016) 11084–11090.
[34] S.V. Dzyuba, R.A. Bartsch, Efficient synthesis of 1-alkyl (aralkyl)-3-methyl (ethyl) imidazolium halides: precursors for room-temperature ionic liquids, J. Heterocycl. Chem. 38 (1) (2001) 265–268.
[35] S.V. Dzyuba, R.A. Bartsch, Influence of structural variations in 1-alkyl (aralkyl)-3-methylimidazolium hexafluorophosphates and bis (trifluoromethylsulfonyl) imides on physical properties of the ionic liquids, ChemPhysChem 3 (2) (2002) 161–166.
[36] M. Thakurathi, E. Gurung, M.M. Cetin, V.D. Thalangamaarachchige, M.F. Mayer, C. Korzeniewski, E.L. Quitevis, The Stokes-Einstein equation and the diffusion of ferrocene in imidazolium-based ionic liquids studied by cyclic voltammetry: effects of cation ion symmetry and alkyl chain length, Electrochim. Acta 259 (2018) 245–252.
[37] S. Lee, S. Niazi, C.D. Yeo, The change in surface properties of magnetic recording media under pulsed laser application, Tribol. Lett. 47 (1) (2012) 57–65.
[38] Michael M. Khonsari, Applied Tribology (Bearing Design and Lubrication), John Wiley & Sons, England, 2001.
[39] W. Zheng, A. Mohammed, L.G. Hines Jr, D. Xiao, O.J. Martinez, R.A. Bartsch, E.L. Quitevis, Effect of cation symmetry on the morphology and physicochemical properties of imidazolium ionic liquids, J. Phys. Chem. B 115 (20) (2011) 6572–6584.
[40] B.R. Hoehn, K. Stahl, K. Michaelis, Lubricant influence on slow speed wear in gears, Goriva maziva: časopis tribol. teh. podmazivanja primjen. tekućih plinovitih goriva inžinjerstvo izgaranja 51 (1) (2012) 17–28.
[41] C. Birleanu, F. Sucala, Friction in low speed lubricated rolling and sliding contacts for alumina, Tribol. Ind. 29 (3–4) (2008) 15–20.
[42] D.R. Lide (Ed.), CRC Handbook of Chemistry and Physics, 7 ed., CRC Press, Boca Raton, 1995.
[43] R.G. Pearson, Hard and soft acids and bases, HSAB, Part 1: fundamental principles, J. Chem. Ed. 45 (1968).
[44] P. Atkins, T. Overton, J. Rourke, M. Weller, F. Armstrong, M. Hagerman, Shriver & Atkins Inorganic Chemistry, Fifth ed., W. H. Freeman and Company, New York, 2010, pp. 138–140.
[45] B. Hammer, The NO+ CO reaction catalyzed by flat, stepped, and edged Pd surfaces, J. Catal. 199 (2) (2001) 171–176.